Thermophysical Properties Mapping of Composites by Lock-in Thermography: Applications on Carbon Fiber Reinforced Plastics

Abdulkareem Alasli[1] · **Ryohei Fujita**[1] · **Hosei Nagano**[1]

Abstract

We propose a versatile method for measuring the thermophysical properties of composites by means of lock-in thermography (LIT) technique. The method is based on analyzing the thermal response distribution induced by periodic laser heating, which enables simultaneous high-spatial-resolution mapping of the effective out-of-plane thermal diffusivity, thermal conductivity, and volumetric heat capacity over the surface of the material. We validate the method using a reference material and demonstrate its capability in visualizing the effective properties of laminated carbon fiber reinforced plastic and carbon fiber reinforced thermoplastic with discontinuous fibers. The results showed that the LIT-based approach has high reproducibility and sensitivity, which allows observing the effect of fiber orientations on the effective properties. The proposed method will be useful for thermal research in composites, defect detection, and for investigating component geometric arrangement effects on the thermophysical properties.

Keywords Composites · Heat capacity · Lock-in thermography · Thermal conductivity · Thermal diffusivity

1 Introduction

Composites have revolutionized the thermal management of a wide variety of engineering applications. This can be seen through the advancement in the thermal control systems of spacecraft, satellites [1], robotics [2], automotive [3], and wearable medical devices [4, 5]. The knowledge of the thermophysical properties, especially the thermal conductivity κ, thermal diffusivity D, and heat capacity c_p, is essential for optimizing the structure and the thermal performance of designed composites.

✉ Hosei Nagano
nagano@mech.nagoya-u.ac.jp

1   Department of Mechanical Systems Engineering, Graduate School of Engineering, Nagoya University, Furo-cho, Chikusa-ku, Nagoya, Aichi 464-8603, Japan

Significant progress has been achieved in the field of thermophysical property measurements [6, 7]. Nevertheless, determining and mapping these properties for a composite, especially fiber and particulate reinforced composites, are still critical issues.

There are two main approaches for determining the effective thermal property of a composite: either by estimating the properties of the constituent materials or by direct measurement. The first approach requires accurate knowledge of the property, the volume fraction, and the geometric distribution of each component [6, 8]. However, having access to such information is difficult due to the large variety of the components with wide range of the property. In addition, the actual geometrical arrangement in the composite is often far from the assumption, especially for fiber reinforced composites [9]. On the other hand, the direct measurement approach is more popular since this approach provides a more reliable and accurate estimation with a wide range of measurement methods. For instance, the direct measurement of the effective κ can be achieved mainly by the steady state and the transient methods [7]. The steady state methods are performed by generating a one-dimensional temperature gradient in the desired measurement direction. Thermocouples are usually used to record the gradient, which in turn is processed numerically based on Fourier's law by the inverse approach to determine the effective κ [10, 11]. This type of measurement techniques requires a long measurement time and its accuracy significantly suffers from the heat loss effect. Alternately, the transient methods, categorized as time domain (TD) and frequency domains (FD) techniques, provide a more rapid and reliable measurement [7]. The TD techniques are based on the time domain temperature response while the FD techniques use the frequency dependence of temperature oscillations, which made FD techniques superior in terms of minimizing the heat loss effect due to its averaging nature [12]. Among the TD and FD techniques, transient plane source (TPS) [13], time domain thermoreflectance (TDTR) [14–16], the 3ω method [17], and frequency domain thermoreflectance (FDTR) [18] are the most adopted methods for the composite measurements. TPS [19–21] and the 3ω method [22] estimate the average value of the effective κ based on the 3D heat flow inside the composite assumed as an infinite medium. On the contrary, TDTR [23, 24] and FDTR [25] allow for mapping the spatial variations in κ within microscale areas.

The direct measurement of the effective D can be estimated through the aforementioned techniques [6]. Yet, the flash [26] and pulse thermography [27] methods are the most commonly used because they provide rapid, non-contact, and inexpensive characteristics [28–31]. They also enable the estimation of D for orthotropic [32] and anisotropic [33] materials and mapping with the aid of an infrared camera [34, 35]. Another well-established technique for measuring and mapping D is the lock-in thermography (LIT) [36–40]. LIT is an active thermal imaging technique that allow to detect the thermal response in a material to a periodic excitation with high temperature resolution [12]. In LIT-based methods, D is typically obtained from the correlation between the phase and/or the amplitude of the temperature modulation and the distance to the periodic heat source and/or its frequency [41]. LIT-based methods have shown notable performance in measuring D of a wide variety of materials, such as metals [42], thin plates and filaments [43], thermoelectric materials [44], and nanocomposites [45]. It was also utilized for assessing D of

moving samples [46] and the fiber direction dependency in carbon fiber reinforced plastics [47, 48].

On the other hand, the effective c_p is measured by a completely different approach. The differential scanning calorimetry [10, 11, 49, 50] and AC calorimetry methods [51, 52] are the leading techniques for composites measurements. However, these types of measurements require the destruction of the material for sampling and are not usable for mapping. It is worth mentioning here that since the three properties are related by Eq. 1, determining two consequently gives the third. Nonetheless, such measurements involve a variety of time-consuming experiments with different sampling requirements and lead to higher combined uncertainties.

$$D = \kappa/\rho c_p \tag{1}$$

In this article, we propose a different approach for simultaneously mapping the out-of-plane thermophysical properties of composite by means of LIT. In addition to D, we show here that LIT also enables mapping of κ and ρc_p with a single apparatus with the aid of laser power-dependent measurements. Since LIT is a non-contact thermal imaging technique, the thermophysical properties of a wide area of single or multiple samples can be mapped without the need for material destruction or the disturbance of heat leakage through temperature probes. The proposed technique can also be utilized for visualizing the effect of the geometric arrangement of components, such as fibers or particles, in composites on the effective thermophysical properties. This will help in improving the thermal structure and production method of the designed composites. For instance, the production method of CFRP has remarkable influence on the distribution and orientations of the high thermal conductive carbon fibers within. This notably affects the homogeneity of the effective thermophysical properties, which are quite challenging to be observed with the conventional measurement methods.

The rest of the paper is organized as follows. The following Sect. 2 explains the principle of the LIT-based measurement technique with modelling and analysis procedure. Section 3 introduces the experimental setup with the measured samples and the experimental conditions. The last section is devoted for validating the method with a composite reference material and demonstrate its usability via measuring and mapping the distribution of the effective thermophysical properties for laminated carbon fiber reinforced plastic and carbon fiber reinforced thermoplastic with discontinuous fibers.

2 Measurement Principle, Modeling and Analysis Procedures

2.1 Measurement Principle

The basic concept of the LIT-based measurement method is illustrated in Fig. 1. The setup consists of an infrared camera connected to a LIT processing system and a function generator. The function generator sends periodic signals at frequency f to the driver of the diode laser and the LIT processing system. The diode laser emits
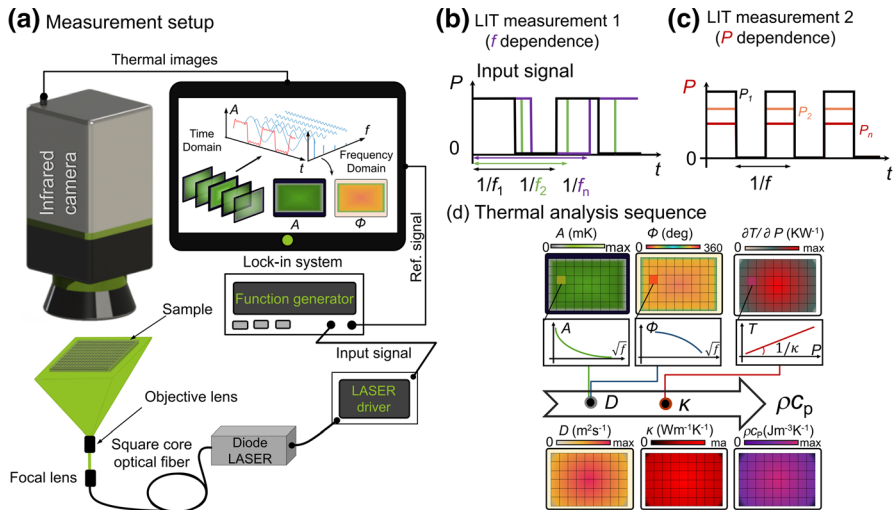
Fig. 1 (a) Schematic diagram of the LIT-based measurement technique. The surface of the sample is heated periodically by the laser at power P and frequency f. The thermal response is imaged by the infrared camera and transferred into amplitude A and phase ϕ at each pixel via the LIT system. (b) and (c) LIT conditions for measuring the f dependence (LIT measurement 1) and P dependence (LIT measurement 2) of the temperature oscillation distribution. In the LIT measurement 1, the periodic laser beam is applied in the form of square wave at different f values while P is fixed. In the LIT measurement 2, the beam is applied at different P values while f is fixed. (d) Sequence of obtaining and mapping the thermal diffusivity D, thermal conductivity κ, and volumetric heat capacity ρc_p by thermal analysis of the LIT images

a modulated laser beam according to the periodic signal with power P. The emitted beam is expanded with an optical setup to ensure a uniform distribution and then incident on the back-side of the infrared opaque sample. The periodic temperature changes $\widetilde{T}$ induced by thermal response is measured on the front-side of the sample by the IR-camera at a specified frame rate and sent to be processed by the LIT system according to the reference signal at f. Consequently, the LIT processing system outputs the lock-in amplitude A and phase ϕ images of $\widetilde{T}$ at the first harmonic ω via the Fourier analysis [12]. The A image shows the spatial distribution of the magnitude of $\widetilde{T}$ due to the transferred heat, while the ϕ image shows the time delay distribution due to the thermal diffusion. Based on the thermal analysis of the obtained A and ϕ images, the properties of interest can be obtained, as detailed in the following section.

2.2 Modeling

To obtain the out-of-plane thermophysical properties of the infrared opaque sample, we derived the f dependence of the induced temperature modulation $\widetilde{T}$ by solving the one-dimensional heat diffusion equation (Eq. 2) in the frequency domain at the steady-periodic condition

$$\frac{\partial T(z,t)}{\partial t} = D\frac{\partial^2 T(z,t)}{\partial z^2} \tag{2}$$

where T is the total temperature of the sample with respect to the constant temperature of the surroundings. As illustrated in Fig. 2a, the modeled system is an isolated slab of thickness d. The boundary conditions of Eq. 2 are

$$-\kappa\frac{\partial T(z,t)}{\partial z}\bigg|_{z=0} = q \tag{3}$$

$$-\kappa\frac{\partial T(z,t)}{\partial z}\bigg|_{z=d} = 0 \tag{4}$$

where q is the periodic heating power per unit area oscillating at f in the form of a square wave with DC shift (Fig. 1b, c), which is defined as [53],

$$q = q_0\left(\frac{1}{2} - \frac{i}{\pi}\sum_{n_{odd}}\frac{1}{n}e^{in\omega t}\right) \tag{5}$$

where q_0 denotes the amplitude of heating and $\omega = 2\pi f$. Since $\widetilde{T}(z,t)$ oscillate at the same harmonics of q and by taking the lock-in component at the first harmonic ω, $T(z,t)$ can be described as,

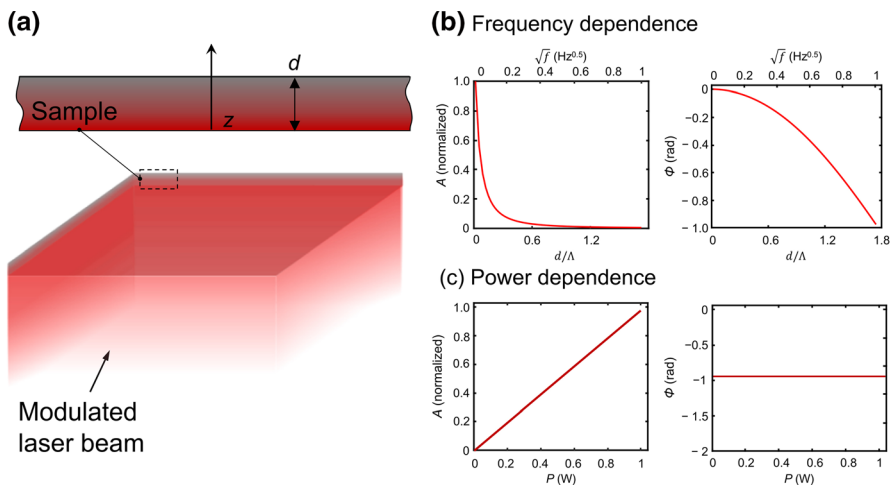$$T(z,t) = T_{\mathrm{DC}}(z) + \widetilde{T}(z)e^{i\omega t} \tag{6}$$

Fig. 2 (a) Schematic of the modeled slab of thickness d. The backside of the sample is heated with a uniform modulated heating source. (b), (c) The theoretical f and P dependence of A and ϕ according to the derived model in Eqs. 9–11, respectively, for $D = 1$ m²s⁻¹, $\kappa = 1$ W·m⁻¹ K.⁻¹, $d = 1$ mm, $f = 1$ Hz (for the P dependence plot), and $P = 1$ W (for the f dependence plot)

By inserting Eq. 6 in Eq. 1, the time dependent component of the differential equation is

$$\left(\lambda^2 - \frac{\partial^2}{\partial^2 z}\right)\widetilde{T}(z) = 0 \tag{7}$$

where the complex number λ is

$$\lambda = \sqrt{\frac{i\omega}{D}} \tag{8}$$

By applying the boundary conditions (Eqs. 2–5), the solution of the temperature modulation $\widetilde{T}(z,t)$ at ω is

$$\widetilde{T}(z,t) = \frac{q_0}{\kappa\sqrt{\frac{2\pi^{\frac{3}{2}}f}{D}}\sinh\left(\sqrt{\frac{2i\pi f}{D}}d\right)}\cosh\left(\sqrt{\frac{2i\pi f}{D}}(d-z)\right)e^{i\left(\omega t - \frac{3\pi}{4}\right)} \tag{9}$$

The amplitude of $\widetilde{T}(z,t)$ is

$$A(z) = \left|\widetilde{T}(z)\right| \tag{10}$$

and its phase

$$\phi = \arg\left[\widetilde{T}(z)\right] \tag{11}$$

2.3 Analysis Procedure and Sequence

Figure 1d summarizes the sequence of the thermal analysis in this method. The effective out-of-plane D can be estimated directly from the f dependence of A and ϕ at each measurement point (pixel) on the surface ($z=d$) of the material through the thermal diffusion length $\Lambda = \sqrt{D/\pi f}$ in Eqs. 10 and 11 [41, 47, 48]. In practice, the f dependence of the out-of-plane A and ϕ data are first obtained by performing a sequence of LIT measurements with sweeping f in a specified range. Then the obtained data are fitted to the theoretical curves with respect to d/Λ (Eqs. 10 and 11, Fig. 2b by considering D as the fitting parameter.

On the other hand, measuring κ and ρc_p by a heat transfer measurement method has the major difficulty of estimating the quantity of q coupled into the material accurately. In practice, quantifying q for laser-based measurement technique can be quite challenging with the current technology due to the power loss between the laser and the sample, which includes optical losses, limited area and the reflectivity of the measured sample [54]. To overcome this problem, we propose a different approach by measuring κ from the q dependence of A. According to the Fourier's law of thermal conduction ($q = -\kappa\nabla T$), κ can be determined not only from q and the temperature gradient ∇T, but also from the derivative of ∇T with respect to q.

In other words, the change in ∇T due to q change is inversely proportional to κ. Based on this concept, we derived the effective out-of-plane κ from the slope of $\partial A/\partial q$ since it is linear (Eq. 10, Fig. 2c) in the absence of the heat loss effect and the temperature dependence of the optical losses. Accordingly, κ can be obtained from Eq. 12 considering $\partial A/\partial q = \partial A/\partial P$ for an infrared opaque material.

$$\kappa = \left| \frac{\cosh\left(\sqrt{\frac{2i\pi f}{D}}(d-z) \right)}{\sqrt{\frac{2\pi^{\frac{3}{2}}f}{D}}\sinh\left(\sqrt{\frac{2i\pi f}{D}}d \right)} \right| \frac{1}{\frac{\partial A}{\partial P}} \tag{12}$$

It is important to emphasize here that the infrared opacity/transparency of the measured sample to the wavelength of the laser beam and the infrared range of the infrared camera affects the correct interpretation of the modulated thermal response signals. This in turn affects the correct estimation of the thermophysical properties through modelling and thermal analyses [55, 56]. Modelling and analyzing infrared semitransparent composites comparing to infrared opaque materials can be quite challenging, especially if the laser absorptivity α and emissivity ε vary over the surface of the composite. This can be easily avoided by uniformly coating the surface of the composite with an infrared opaque thin layer of a black-body paint of α and $\varepsilon \approx 1$. Nevertheless, this might not be always applicable such as in the case of flexible composites under stretching or thin film composites. For such cases, the more complex modelling considering the effect of the infrared transparency is required [57, 58].

To obtain the thermophysical properties, two LIT measurement sets are performed. In LIT measurement set 1 (f dependence measurement, Fig. 1b), f of the modulated laser beam is swept over a specified range by keeping P constant, while in LIT measurement set 2 (P dependence measurement, Fig 1c), P is changed in constant intervals by keeping f constant. Each pixel of the LIT images is then analyzed using Eqs. 10, 11 and 12 to determine and map the D, κ, and ρc_{p} (Fig. 1d). D is first obtained by fitting A and ϕ of LIT measurement set 1 (f dependence) to Eqs. 9 and 10 at the front-side of the sample ($z=d$). κ is then obtained from the slope of the amplitude A of LIT measurement set 2 with respect to P at the front-side of the sample ($z=d$) with the knowledge of D with Eq. 12. Finally, the obtained D and κ are substituted into Eq. 1 to calculate ρc_{p}.

3 Samples, Measurement Setup and Experimental Conditions

3.1 Samples

To demonstrate the usability of the proposed technique, we measured and mapped the thermophysical properties of three different materials. First, Al_2O_3-TiC ceramic composite reference material is used for validation, which is the same as the National Metrology of Japan (NMIJ) certified reference material of $D = 9.51 \pm 6.1\% \mathrm{mm^2 \cdot s^{-1}}$

and $\kappa = 21.1 \pm 15\% \, \mathrm{W} \cdot \mathrm{m}^{-1} \cdot \mathrm{K}^{-1}$ at 300 K [59, 60]. Second, a carbon fiber reinforced plastic (CFRP) sample is used for demonstrating measuring the effective thermophysical properties of a composite. The sample is fabricated by laminating pre-impregnated ("prepreg") sheets of carbon fiber/epoxy (T700/#2592) with $[45/-45]_{4S}$ structure and curing them in an autoclave [41]. The evaluation of the properties is based on a 25 mm × 25 mm sample at a thickness of 2.40 mm, as shown in Fig. 3a and c. Third, a carbon fiber reinforced plastic (CFRTP) with short discontinuous fibers sample is measured for evaluating the effect of fiber orientation and distribution on the effective thermophysical properties. The sample is a cut-out from a plate prepared with a polyamide-6 resin and PAN-based discontinuous carbon fibers by the Carbon-Long Fiber Thermoplastic-Direct (C-LFT-D) method [61]. In this method, the fiber orientation is biased due to nonuniform resin flow during the press compaction, as it can be traced via XCT images shown in Fig. 3e and f. The sample size is 36 × 29 mm with a thickness that varies from 2.91 to 3.45 mm, as displayed in Fig. 3b and d.

3.2 Measurement Setup

The temperature response from the samples is recorded by a science-grade Thermo Hawak H9000 infrared thermography system (InfRec, Nippon Avionics Co., Ltd., Japan). The infrared camera is equipped with a focal plane array consisting of 640 × 512 pixels of InSb quantum well-infrared photodetector. The spectral detection ranges from 2.0 to 5.7 µm at a maximum frame rate of 205 Hz and temperature resolution of 25 mK. With a 1 × lens fixed on the infrared
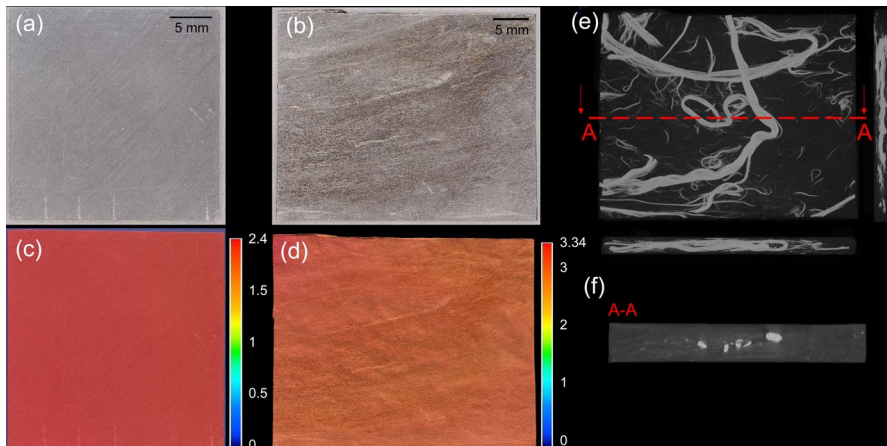

Fig. 3 Images of the measured (a) carbon fiber reinforced plastic (CFRP) and (b) carbon fiber reinforced thermoplastic (CFRTP) samples with, respectively, the corresponding (c) and (d) thickness profiles obtained by 3D optical profilometer (Keyence VR-6000; Keyence Co., Japan). (e) X-ray computed tomography (CT) image of the CFRTP sample captured by microfocus X-ray CT system (inspeXio SMX-225CT FPD HR, SHIMADZU Co, Ltd. Japan) with (f) cross section at the middle of the sample. Cu-plated carbon fiber bundles are added at 3 wt% as a tracer for X-ray CT visualization

camera, a spatial pixel resolution of ~ 80 μm is reached. The diode laser module used for heating the back-side of the free-standing sample is BrixX® 445-2500 HP (Omicron, Laserprodukte GmbH, Germany) with a wave length of 445 ± 5 nm and rise/fall time of < 200 ns. The output power of the laser (maximum 2500 mW) is controlled by the laser driver. The laser beam is transmitted from the module through a square-core (150 μm × 150 μm) fiber patch cable with a variable focal lens. Since our model assumes one-dimensional heat wave propagation, the whole surface of the measured sample is heated after expanding the laser beam with an objective lens (OptoSigma, PAL-20-L-A, Japan). The uniformity of the beam is ensured by a beam quality analyzer (BC106N-VIS/M, Thorlabs), as presented in Fig. 4a. Moreover, the linearity and equal power stepping of the applied beam for LIT measurement 2 is also verified by a calibrated optical power detector (Newport, 918D-SL, OD3 Attenuator), as plotted in Fig. 4b.

3.3 Experimental Conditions

The experimental conditions of the conducted LIT measurements1 and 2 are listed in Table 1. The samples are coated before measurements with a black-body paint (JSC 3, Japan Sensor Corp.) to enhance and unify α and $\varepsilon > 0.94$. The sample is suspended in air horizontally to suppress the natural convection effect with a set of plastic wires of low κ. The measurements were performed with a frame rate of 76.13 Hz at room temperature and atmospheric pressure.
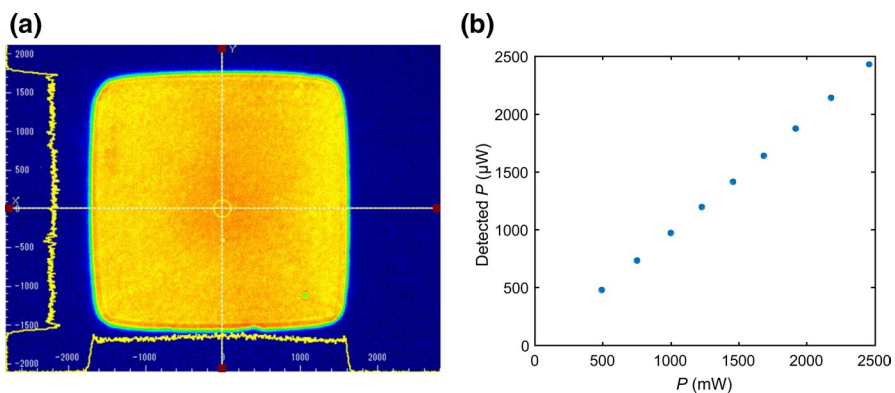

Fig. 4 The profile and the measured laser beam power. (a) The uniformity across the beam profile is mapped and verified with less than 5% deviation from the maximum intensity at the center before being incident on the back-side of the sample. (b) The linear responses of the beam intensity to the out-put laser P change via the laser driver at different values. The intensity is measured after passing the beam through the attenuator to protect the photodiode sensor (reduced by ~ 1000×)

Table 1 Experimental conditions for LIT measurements 1 and 2

Sample	Set1 (f dependence)			Set2 (P dependence)		
	Al_2O_3-TiC	CFRP	CFRTP	Al_2O_3-TiC	CFRP	CFRTP
P (W)	2.5			0.5–2.5		
f (Hz)	1–10	0.02–0.15	0.02–0.15	1	0.02	0.02
Meas. periods	> 500	50	50	> 500	50	50

4 Result and Discussion

4.1 Method Validation

To validate the LIT-based method, we have performed the LIT measurements 1 and 2 on the reference material. Figure 5a and b show, respectively, the f dependence of A and ϕ and P dependence of A and ϕ thermal images and the corresponding fitted data taken at different pixels on the surface of the sample. In both measurements, clear laser-induced temperature modulation signals appear in the vicinity of the sample. A images show relatively uniform distribution with a slight gradient towards the edges. This can be attributed to the deviation in the beam profile intensity (Fig. 4a) and to the heat loss and edge effects. On the other hand, ϕ images show a more detailed description of the sample. Surprisingly, the effect of the holding plastic wire can be realized clearly in the images, especially at higher f. This can be attributed to the lower D of the wire and the interfacial thermal resistance, which causes a shift in ϕ [62]. Moreover, increasing f decreases the thermal diffusion length Λ, which is reflected in improving the resolution of the thermal images, especially for ϕ images since it only depends on $1/\Lambda$ at a fixed thickness (Eqs. 9 and 10) [63]. In contrast, increasing f also increases the noise to signal ratio. Therefore, the f range should be selected by counter balancing these two effects. Furthermore, the fitted curves show a good agreement between the experimental data and the theoretical model. A (ϕ) values exhibit exponential decay (monotonic increase) with $\sqrt{f}$ at the measured points. These behaviors are consistent with Eqs. 10 and 11 (Fig. 2b). On the other hand, A (ϕ) values reveal linear growth (no change) with P at the same points. This supports the assumption of the linear dependency of A with respect to P (Eq. 10 and Fig. 2c).

Figures 6a–c show the out-of-plane D, κ, and ρc_p distribution and the representative histograms mapped over the surface of the sample, which are obtained by analyzing the LIT images according to Sect. 2.3. The previously realized beam deviation and holding wires effects in A and ϕ images are reflected clearly in the obtained properties images. Quantitatively, the histograms show, respectively, that the ranges of the mapped D, κ, and ρc_p are concentrated near 1.00×10^{-5} m²·s⁻¹, 21 W·m⁻¹·K⁻¹, and 2.1×10^6 J·m⁻³·K⁻¹, which are consistent with the given reference values within 10–15% deviation. The deviation in the values is mainly originated from the observed deviations in the f dependence images of A and ϕ, and P dependence images of A (Fig. 5a–c). This further emphasizes the importance of
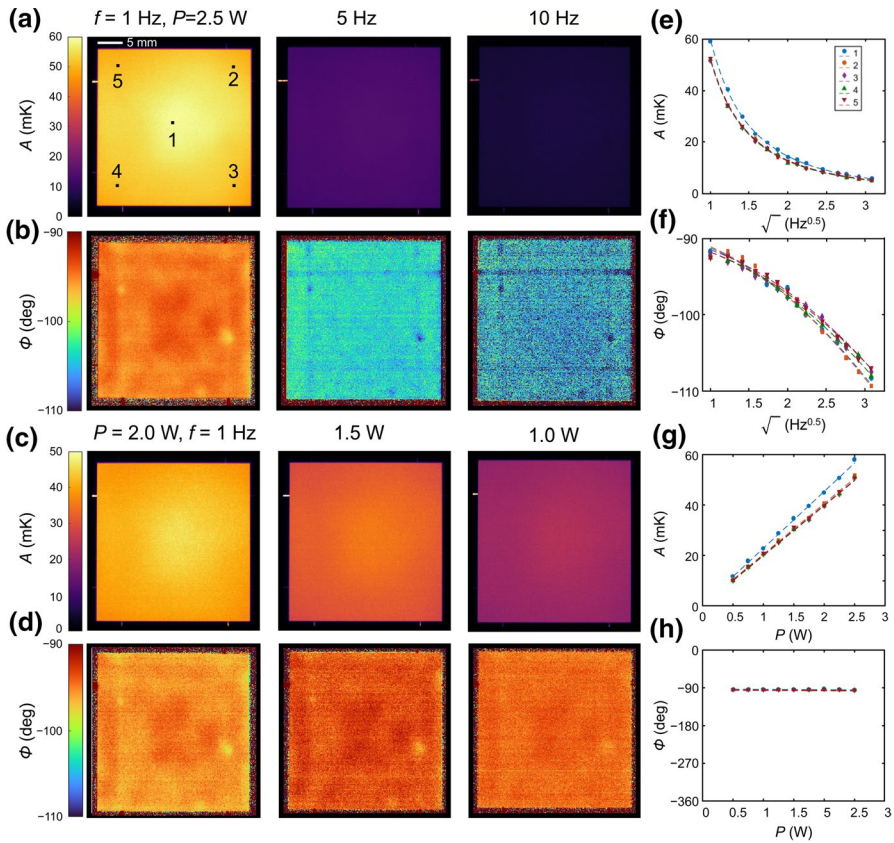
Fig. 5 f dependence of the (a) amplitude A and (b) phase ϕ images at $P=2.5$ W and P dependence of (c) A and (d) ϕ at $f=1$ Hz for the Al_2O_3-TiC reference sample. (e)-(h) are, respectively, the corresponding measured data taken at different pixels on the surface of the sample. The dashed lines represent the fitting results using Eqs. 10 and 11

ensuring the uniformity of the laser beam profile and minimizing the heat loss effect for high accuracy measurements. On the other hand, this also indicates the high sensitivity of the LIT-based method, which has notable potential for defect recognition [64] and visualizing the effect of the component arrangement in a composite on its effective thermophysical properties, as it will be demonstrated later.

4.2 Mapping Effective Thermophysical Properties of Laminated CFRP

To demonstrate the capability of the proposed method in mapping the effective D, κ, and ρc_p of a composite, we measured the laminated CFRP sample. Figure 7a–c show, respectively, the mapped out-of-plane D, κ, and ρc_p and the corresponding histograms based on the thermal images of LIT measurements 1 and 2 (see Appendix A, Fig. 9). A relatively uniform distribution of the effective D, κ, and ρc_p can be realized over the surface of the sample. The histograms confirm that
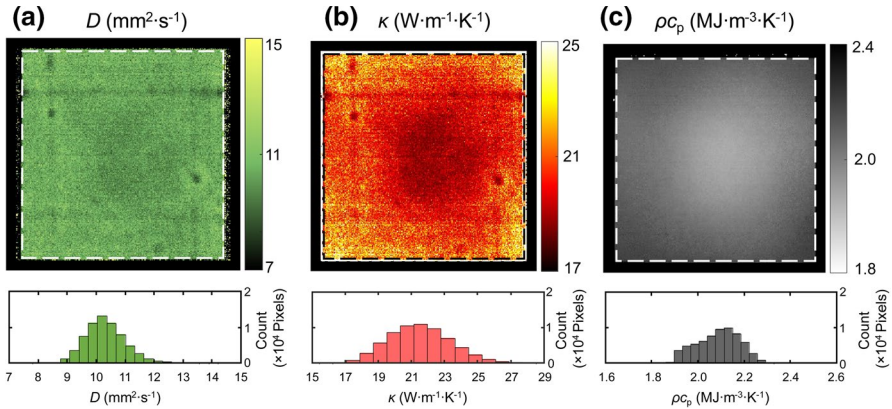
Fig. 6 The effective (a) D, (b) κ, and (c) ρc_p distributions over the surface (dashed rectangles) of the Al$_2$O$_3$-TiC sample at spatial resolution of ~80 μm per pixel with the representative histograms at $T = 300$ K. D was obtained from the f dependence images of A and ϕ by fitting at each pixel. κ was estimated from the P dependence images of A by fitting at each pixel. ρc_p image was derived from dividing κ image by D image
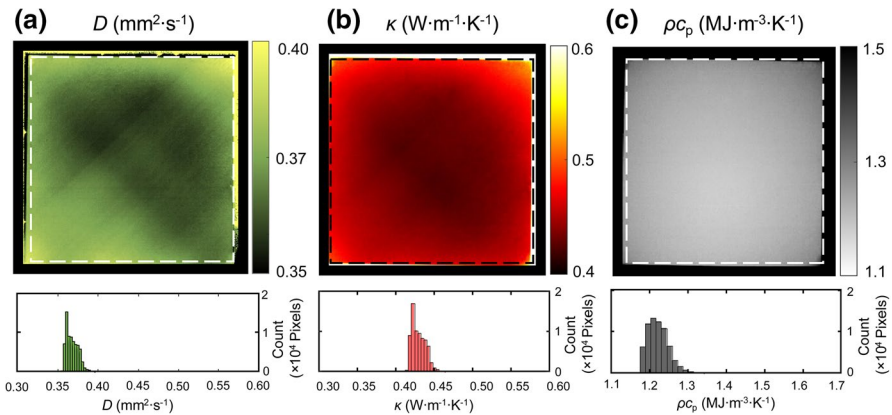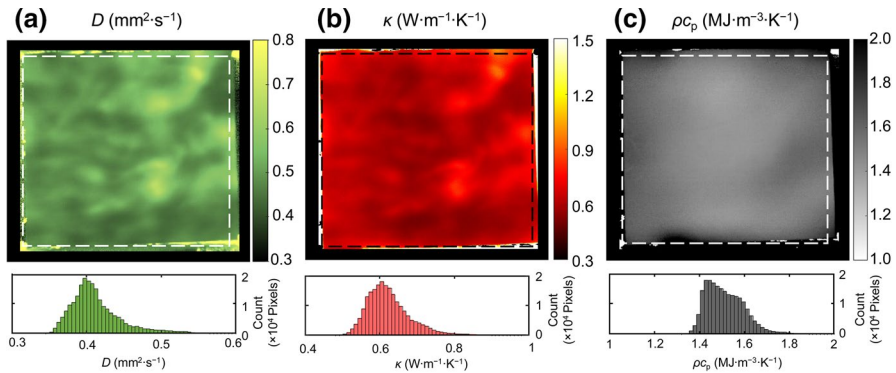

Fig. 7 The effective (a) D, (b) κ, and (c) ρc_p distributions over the surface (dashed rectangles) of the CFRP sample at spatial resolution of ~80 μm per pixel with the representative histograms at $T = 300$ K

the estimated values of the effective D, κ and ρc_p are located at 0.36×10^{-6} m^2·s^{-1}, 0.42 W·m^{-1}·K^{-1}, and 1.23×10^6 J·m^{-3}·K^{-1}, respectively, within a narrow range of 6–8%. These values are consistent with the reported result in the literature [65]. Importantly, the effect of the fiber distribution near the surface can be observed in D and κ images as a notable contrast in the same direction of the fiber orientations (45°/−45°). The high difference (~30×) between κ of the resin (0.31 W·m^{-1}·K^{-1}) [65] and the longitudinal κ of the carbon fibers (9.38 W·m^{-1}·K^{-1}) [66] is the main reason behind this behavior. On the other hand, no similar distinction can be realized in the ρc_p image since the values of the resin (1.30×10^6 J·m^{-3}·K^{-1}) [65] and the fiber (1.36×10^6 J·m^{-3}·K^{-1}) [66] are almost equivalent. These results further

Fig. 8 The effective (a) D, (b) κ, and (c) ρc_p distributions over the surface (dashed rectangles) of the CFRTP sample at spatial resolution of ~ 80 µm per pixel with the representative histograms at $T = 300$ K

confirm the validity of the LIT-based measurement technique as a tool for investigating the thermophysical properties of composites.

4.3 Mapping Effective Thermophysical Properties of CFRTP

Figures 8a–c illustrate the mapped thermophysical properties of the CFRTP sample with the corresponding histograms estimated from the LIT images (shown in Appendix A, Fig. 10) by considering the mapped thickness values (Fig. 3d). In contrast to the laminated CFRP sample, the properties of the CFRTP sample showed wider wavy distribution with a higher average value of the effective thermophysical properties. The average value of the effective D, κ and ρc_p are around 0.4×10^{-6} m^2·s^{-1}, 0.6 W·m^{-1}·K^{-1}, and 1.5×10^6 J·m^{-3}·K^{-1}, which are consistent with the reported data [65]. The images show more wavy variation in the D and κ images across different sample regions than of ρc_p image. The distribution of D and κ is originated from the biased orientation of the discontinuous carbon fiber resulting from the nonuniform resin flow during the press. The fibers with a significantly higher longitudinal κ act as a complex network of thermal bridges within the sample. The fibers, tended to align in the out-of-plane direction, are contributing more to transferring heat in that direction. On the other hand, since ρc_p does not depend on the orientation of the fibers, a notable difference between the values of the resin (2.18×10^6 J·m^{-3}·K^{-1}) and the fiber (1.36×10^6 J·m^{-3}·K^{-1}) can indicate where the fibers are more concentrated within the sample. This does not necessarily align with D or κ images since they also have an inherent fiber orientations effect. This information is usually difficult to obtain by conventional methods such as ultrasonic inspection or X-ray CT visualization techniques (Fig. 3e and f). It is worth noting here that the added Cu-plated

carbon fibers bundles for X-ray CT visualization do not seem to have a notable additional effect on the effective properties since they only represent a small number of the fibers (3% wt). These observations emphasize the capability of the proposed method for visualizing the effect of the geometric arrangement of the components on the effective thermophysical properties in a composite.

5 Conclusions

In summary, we have proposed and demonstrated a new method for measuring and mapping the effective out-of-plane D, κ, and ρc_p of a composite by means of LIT. The thermophysical properties are determined through the thermal analysis of the imaged out-of-plane thermal waves diffusion induced by laser surface heating, enabling systematic, sensitive, and reliable non-contact measurement. The method is validated with a reference material and measurements on CFRP and CFRTP samples showed that the method could also be used for visualizing the effect of the arrangement of the component in a composite on the effective thermophysical properties, which are usually difficult to be observed by the conventional methods. Although the mapping spatial resolution is ~ 80 μm per pixel in the current setup, it can be easily increased with a high magnification lens, opening a way to characterize micro/nano composites. Furthermore, the mapped properties images can be utilized with the aid of machine-learning-based algorithms [67] to further optimize the structure, the thermal performance, and the production method of designed composites. Thus, we anticipate that the LIT-based measurement method will participate in advancing thermal science research for composites as well as materials.

Appendix A: Thermal Images of the Frequency and Power Dependences of the Temperature Modulation for Carbon Fiber Reinforced Plastics Samples
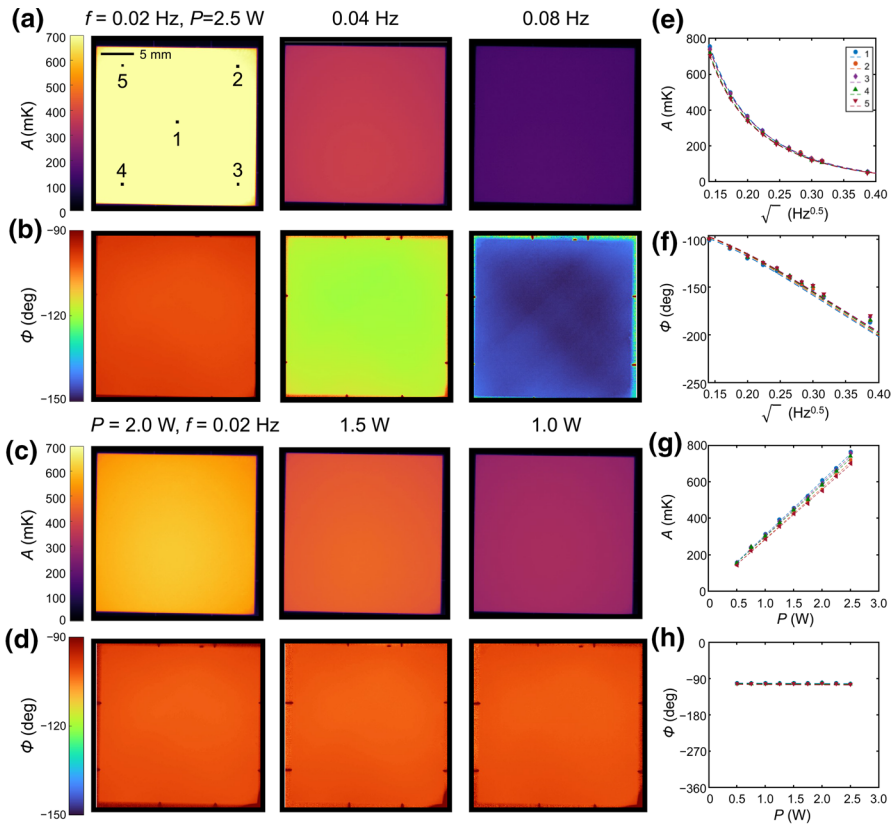
See Figs. 9 and 10.

Fig. 9 f dependence of the (a) A and (b) ϕ images at $P = 2.5$ W and P dependence of (c) A and (d) ϕ at $f = 1$ Hz for the CFRP sample. (e)–(h) are, respectively, the corresponding measured data taken at different pixels on the surface of the sample. The dashed lines represent the fitting results using Eqs. 10 and 11
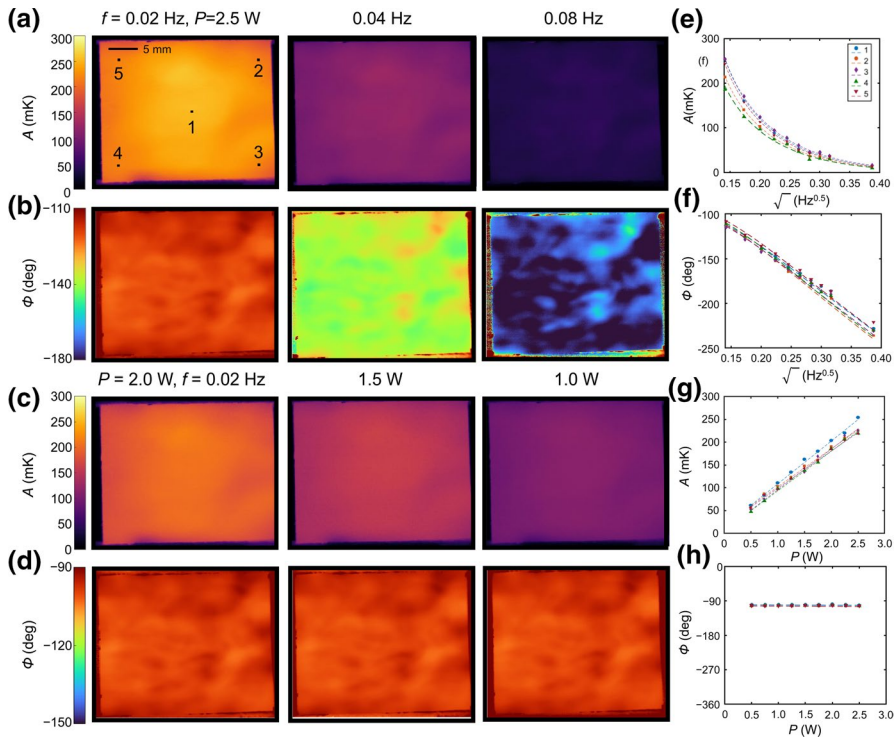
Fig. 10 f dependence of the (a) A and (b) ϕ images at $P = 2.5$ W and P dependence of (c) A and (d) ϕ at $f = 1$ Hz for the CFRTP sample. (e)–(h) are, respectively, the corresponding measured data taken at different pixels on the surface of the sample. The dashed lines represent the fitting results using Eqs. 10 and 11

Author Contributions Abdulkareem Alasli: Conceptualization, Methodology, Investigation, Formal analysis, preparing figures, Writing—Original Draft. Ryohei Fujita: Conceptualization, Investigation, Resources, Writing—Review & Editing. Hosei Nagano: Conceptualization, Resources, Writing—Review & Editing, Supervision, Funding acquisition.

Data Availability The datasets generated during and analysed during the current study are available from the corresponding author on reasonable request.

Declarations

Conflict of interest The authors declare that they have no known competing financial interests or personal relationships that could have appeared to influence the work reported in this article.

References

1. I. Levchenko, K. Bazaka, T. Belmonte, M. Keidar, S. Xu, Adv. Mater. **30**, 1 (2018). https://doi.org/10.1002/adma.201802201
2. E. Sevinchan, I. Dincer, H. Lang, Appl. Therm. Eng. **140**, 799 (2018). https://doi.org/10.1016/j.applthermaleng.2018.04.132
3. M. Subramanian, A.T. Hoang, B. Kalidasan, S. Nižetić, J.M. Solomon, D. Balasubramanian, C. Subramanian, G. Thenmozhi, H. Metghalchi, X.P. Nguyen, J. Clean. Prod. **322**, 129079 (2021). https://doi.org/10.1016/j.jclepro.2021.129079
4. A.S. Farooq, P. Zhang, Compos. Part A Appl. Sci. Manuf. **142**, 106249 (2021). https://doi.org/10.1016/j.compositesa.2020.106249
5. R. Bahru, A.A. Hamzah, M.A. Mohamed, Int. J. Energy Res. **45**, 1517 (2021). https://doi.org/10.1002/er.6031
6. L. Qiu, N. Zhu, Y. Feng, E.E. Michaelides, G. Żyła, D. Jing, X. Zhang, P.M. Norris, C.N. Markides, O. Mahian, Phys. Rep. **843**, 1 (2020). https://doi.org/10.1016/j.physrep.2019.12.001
7. A. Palacios, L. Cong, M.E. Navarro, Y. Ding, C. Barreneche, Renew. Sustain. Energy Rev. **108**, 32 (2019). https://doi.org/10.1016/j.rser.2019.03.020
8. A.J. Whittaker, R. Taylor, J.E. Enderby, Proc. R. Soc. Lond. A **430**, 199 (1990). https://doi.org/10.1098/rspa.1990.0088
9. A. Dasgupta, R.K. Agarwal, J. Compos. Mater. **26**, 2736 (1992). https://doi.org/10.1177/002199839202601806
10. R.D. Sweeting, X.L. Liu, Compos. Part A Appl. Sci. Manuf. **35**, 933 (2004). https://doi.org/10.1016/j.compositesa.2004.01.008
11. Y. Guo, Z. Lyu, X. Yang, Y. Lu, K. Ruan, Y. Wu, J. Kong, J. Gu, Compos. Part B Eng. **164**, 732 (2019). https://doi.org/10.1016/j.compositesb.2019.01.099
12. O. Breitenstein, W. Warta, M. Langenkamp, *Lock-in Thermography: Basics and Use for Evaluating Electronic Devices and Materials* (Springer, Berlin/Heidelberg, Germany, 2010)
13. S.E. Gustafsson, Rev. Sci. Instrum. **62**, 797 (1991). https://doi.org/10.1063/1.1142087
14. C.A. Paddock, G.L. Eesley, J. Appl. Phys. **60**, 285 (1986). https://doi.org/10.1063/1.337642
15. W.S. Capinski, H.J. Maris, T. Ruf, M. Cardona, K. Ploog, D.S. Katzer, Phys. Rev. B **59**, 8105 (1999). https://doi.org/10.1103/PhysRevB.59.8105
16. D.G. Cahill, Rev. Sci. Instrum. **75**, 5119 (2004). https://doi.org/10.1063/1.1819431
17. D.G. Cahill, Rev. Sci. Instrum. **61**, 802 (1990). https://doi.org/10.1063/1.1141498
18. A.J. Schmidt, R. Cheaito, M. Chiesa, Rev. Sci. Instrum. **80**, 094901 (2009). https://doi.org/10.1063/1.3212673
19. E. Karawacki, B.M. Suleiman, I. Ul-Haq, B.T. Nhi, Rev. Sci. Instrum. **63**, 4390 (1992). https://doi.org/10.1063/1.1143739
20. K. Singh, N.S. Saxena, M.S. Sreekala, S. Thomas, J. Appl. Polym. Sci. **89**, 3458 (2003). https://doi.org/10.1002/app.12557
21. R. Mangal, N.S. Saxena, M.S. Sreekala, S. Thomas, K. Singh, Mater. Sci. Eng. A **339**, 281 (2003). https://doi.org/10.1016/S0921-5093(02)00166-1
22. T. Tian, K.D. Cole, Int. J. Heat Mass Transf. **55**, 6530 (2012). https://doi.org/10.1016/j.ijheatmasstransfer.2012.06.059
23. E.K. Pek, J. Brethauer, D.G. Cahill, J. Nucl. Mater. **542**, 152519 (2020). https://doi.org/10.1016/j.jnucmat.2020.152519
24. D.H. Olson, J.T. Gaskins, J.A. Tomko, E.J. Opila, R.A. Golden, G.J.K. Harrington, A.L. Chamberlain, P.E. Hopkins, Scr. Mater. **177**, 214 (2020). https://doi.org/10.1016/j.scriptamat.2019.10.027

25. J. Yang, T. Sato, P. Czubarow, A. Schmidt, J. Heat Transfer (2015). https://doi.org/10.1115/1.4029012

26. W.J. Parker, R.J. Jenkins, C.P. Butler, G.L. Abbott, J. Appl. Phys. **32**, 1679 (1961). https://doi.org/10.1063/1.1728417

27. T. Kostroun, M. Dvořák, Materials (Basel). **14**, 533 (2021). https://doi.org/10.3390/ma14030533

28. D.L. Ellis, D.L. McDanels, Metall. Trans. A **24**, 43 (1993). https://doi.org/10.1007/BF02669601

29. Y.H. Zhao, Z.K. Wu, S.L. Bai, Int. J. Heat Mass Transf. **101**, 470 (2016). https://doi.org/10.1016/j.ijheatmasstransfer.2016.05.068

30. W.P. Adamczyk, S. Pawlak, Z. Ostrowski, Meas. J. Int. Meas. Confed. **124**, 147 (2018). https://doi.org/10.1016/j.measurement.2018.04.022

31. L. Wang, M. Gandorfer, T. Selvam, W. Schwieger, Mater. Lett. **221**, 322 (2018). https://doi.org/10.1016/j.ijthermalsci.2017.11.017

32. L. Gaverina, A. Sommier, J.L. Battaglia, J.C. Batsale, C. Pradere, Int. J. Therm. Sci. **125**, 142 (2018). https://doi.org/10.1016/j.ijthermalsci.2017.11.017

33. L. Gaverina, M. Bensalem, A. Bedoya, J. González, A. Sommier, J.L. Battaglia, A. Salazar, A. Mendioroz, A. Oleaga, J.C. Batsale, C. Pradere, Int. J. Therm. Sci. **145**, 106000 (2019)

34. M. Larciprete, N. Orazi, Y.S. Gloy, S. Paoloni, C. Sibilia, R. Li-Voti, Sensors **22**, 940 (2022). https://doi.org/10.3390/s22030940

35. M. Gresil, Z. Wang, Q.A. Poutrel, C. Soutis, Sci. Rep. **7**, 1 (2017). https://doi.org/10.1038/s41598-017-05866-0

36. M. Wandelt and W. Roetzel, in Proc. 1996 Int. Conf. Quant. InfraRed Thermogr. (QIRT Council, 1996). https://doi.org/10.21611/qirt.1996.031

37. A. Salazar, A. Mendioroz, R. Fuente, Appl. Phys. Lett. **95**, 121905 (2009). https://doi.org/10.1063/1.3236782

38. P. Cielo, L.A. Utracki, M. Lamontagne, Can. J. Phys. **64**, 1172 (1986). https://doi.org/10.1139/p86-204

39. K. Strzałkowski, M. Streza, M. Pawlak, Measurement **64**, 64 (2015). https://doi.org/10.1016/j.measurement.2014.12.040

40. G. Dell'Avvocato, D. Palumbo, M. E. Palmieri, and U. Galietti, in Thermosense Therm. Infrared Appl. XLIV, edited by N. P. Avdelidis and A. Mendioroz (SPIE, 2022), p. 8. https://doi.org/10.1117/12.2618810

41. T. Ishizaki, H. Nagano, Infrared Phys. Technol. **99**, 248 (2019). https://doi.org/10.1016/j.infrared.2019.04.023

42. P.W. Nolte, T. Malvisalo, F. Wagner, S. Schweizer, Quant. Infrared Thermogr. J. **14**, 218 (2017). https://doi.org/10.1080/17686733.2017.1329777

43. A. Mendioroz, R. Fuente-Dacal, E. Apiñaniz, A. Salazar, Rev. Sci. Instrum. **80**, 074904 (2009). https://doi.org/10.1063/1.3176467

44. A. Alasli, A. Miura, R. Iguchi, H. Nagano, K. Uchida, Sci. Technol. Adv. Mater. Methods **1**, 162 (2021). https://doi.org/10.1080/27660400.2021.1963642

45. L.I. Giri, S. Tuli, M. Sharma, P. Bugnon, H. Berger, A. Magrez, Mater. Lett. **115**, 106 (2014). https://doi.org/10.1016/j.matlet.2013.10.042

46. A. Salazar, L. Zamanillo, M. Colom, A. Mendioroz, U. Galietti, A. Sommier, J.C. Batsale, C. Pradere, Quant. Infrared Thermogr. J. **17**, 279 (2020). https://doi.org/10.1080/17686733.2019.1655248

47. R. Fujita, H. Nagano, Compos. Sci. Technol. **140**, 116 (2017). https://doi.org/10.1016/j.compscitech.2016.12.006

48. K. Miyachi, Y. Muranaka, S. Nonaka, A. Ueno, H. Nagano, Infrared Phys. Technol. **115**, 103743 (2021). https://doi.org/10.1016/j.infrared.2021.103743

49. H.B. Shim, M.K. Seo, S.J. Park, J. Mater. Sci. **37**, 1881 (2002). https://doi.org/10.1023/A:1014959603892

50. J. Diani, K. Gall, Polym Eng Sci **46**, 486–492 (2006). https://doi.org/10.1002/pen.20497

51. Y. Kraftmakher, Phys. Rep. **356**, 1 (2002). https://doi.org/10.1016/S0370-1573(01)00031-X

52. L.A. Rosenthal, Rev. Sci. Instrum. **32**, 1033 (1961). https://doi.org/10.1063/1.1717607

53. H.S. Carslaw, J. Jaeger, *Conduction of Heat in Solids* (Clarendon press, Oxford, UK, 1992)

54. A. Wolf, P. Pohl, R. Brendel, J. Appl. Phys. **96**, 6306 (2004). https://doi.org/10.1063/1.1811390

55. H.G. Walther, U. Seidel, W. Karpen, G. Busse, Rev. Sci. Instrum. **63**, 5479 (1992). https://doi.org/10.1063/1.1143372

56. S. André, B. Rémy, D. Maillet, A. Degiovanni, J.J. Serra, J. Appl. Phys. **96**, 2566 (2004). https://doi.org/10.1063/1.1774260

57. M. Pawlak, M. Streza, C. Morari, K. Strzałkowski, M. Depriester, M. Chirtoc, Meas. Sci. Technol. **28**, 025008 (2017). https://doi.org/10.1088/1361-6501/aa4f69
58. A. Philipp, N.W. Pech-May, B.A.F. Kopera, A.M. Lechner, S. Rosenfeldt, M. Retsch, Anal. Chem. **91**, 8476 (2019). https://doi.org/10.1021/acs.analchem.9b01583
59. NMIJ, Certified Reference Materials Catalog 2021–2022, https://unit.aist.go.jp/qualmanmet/refmate/pdf/CRM_Catalog_(JE)_2021-2022.pdf. Accessed 19 Jul 2022
60. Nippon Tungsten Co., Ltd, https://www.nittan.co.jp/products/ceramicsmaterial_002_004.html. Accessed 19 Jul 2022
61. T. Ishikawa, K. Amaoka, Y. Masubuchi, T. Yamamoto, A. Yamanaka, M. Arai, J. Takahashi, Compos. Sci. Technol. **155**, 221 (2018). https://doi.org/10.1016/j.compscitech.2017.09.015
62. T. Ishizaki, T. Igami, H. Nagano, Rev. Sci. Instrum. **91**, 064901 (2020). https://doi.org/10.1063/5.0002937
63. E. S. Watson and M. J. O'Neill, (1962). https://patents.google.com/patent/US3263484
64. I. Jorge Aldave, P. Venegas Bosom, L. Vega González, I.L. De Santiago, B. Vollheim, L. Krausz, M. Georges, Infrared Phys. Technol. **61**, 167 (2013). https://doi.org/10.1016/j.infrared.2013.07.009
65. Japan Society of Thermophysical Properties, Thermophysical Properties Handbook, 2008th ed. (Tokyo, 2008).
66. Z. Ning, R. Liu, R.F. Elhajjar, F. Wang, Compos. Part B Eng. **114**, 247 (2017). https://doi.org/10.1016/j.compositesb.2017.01.036
67. H. Wei, S. Zhao, Q. Rong, H. Bao, Int. J. Heat Mass Transf. **127**, 908 (2018). https://doi.org/10.1016/j.ijheatmasstransfer.2018.08.082

Publisher's Note Springer Nature remains neutral with regard to jurisdictional claims in published maps and institutional affiliations.